


Disentangling Spin, Anomalous, and Planar Hall Effects in Ferromagnet–Heavy-Metal Nanostructures

Inge Groen¹, Van Tuong Pham^{1,2}, Naëmi Leo¹, Alain Marty², Luis E. Hueso^{1,3}, and Félix Casanova^{1,3,*}

¹*CIC nanoGUNE BRTA, 20018 Donostia-San Sebastian, Basque Country, Spain*

²*University Grenoble Alpes, CEA, CNRS, G-INP, Spintec, 38054 Grenoble, France*

³*IKERBASQUE, Basque Foundation for Science, 48013 Bilbao, Basque Country, Spain*

 (Received 11 November 2020; revised 26 January 2021; accepted 10 March 2021; published 5 April 2021)

Ferromagnet (FM)–heavy-metal (HM) nanostructures can be used for magnetic state readout in the proposed magnetoelectric spin-orbit logic by locally injecting a spin-polarized current and measuring the spin-to-charge conversion via the spin Hall effect. However, this local configuration is prone to spurious signals. Here, we address spurious Hall effects that can contaminate the spin Hall signal in these FM/HM T-shaped nanostructures. The most pronounced Hall effects in our $\text{Co}_{50}\text{Fe}_{50}/\text{Pt}$ nanostructures are the planar Hall effect and the anomalous Hall effect generated in the ferromagnetic nanowire. We find that the planar Hall effect, induced by misalignment between magnetization and current direction in the ferromagnetic wire, is manifested as a shift in the measured baseline resistance, but does not alter the spin Hall signal. In contrast, the anomalous Hall effect, arising from the charge-current distribution within the FM, adds to the spin Hall signal. However, the effect can be made insignificant by minimizing the shunting effect via proper design of the device. We conclude that local spin injection in FM/HM nanostructures is a suitable tool for measuring spin Hall signals and, therefore, a valid method for magnetic state readout in prospective spin-based logic.

DOI: [10.1103/PhysRevApplied.15.044010](https://doi.org/10.1103/PhysRevApplied.15.044010)

I. INTRODUCTION

Spin orbitronics [1] is an expanding field in condensed matter physics that aims to utilize different phenomena in magnetism and spintronics caused by the spin-orbit coupling (SOC) [2–5]. One of the most studied phenomena in spin orbitronics is the spin Hall effect (SHE), occurring in heavy metals (HM) with a strong bulk SOC, such as Pt, Ta, and W [6–11]. The SHE allows for interconversion between charge currents and spin currents [6] and has a strong potential to be harnessed for energy-efficient logic and memory tasks for processing of information [5,12–15]. The SHE converts a charge current into a spin current and can be used to write magnetic memory states [16,17]. The reciprocal effect (inverse SHE, ISHE), responsible for the conversion of a spin current into a charge current, can achieve reading of magnetic memory states [13,18]. Particularly, the readout of nonvolatile magnetic states via the inverse SHE is one of the main components of the magnetoelectric spin-orbit (MESO) logic, because it generates an electromotive force (voltage) and a current that can be used to cascade different elements of the logic-built-in-memory architecture. In contrast, the magnetic state

readout by magnetoresistance techniques [19,20], widely used in our modern technology, do not have the ability to drive other circuit elements. The MESO logic is computed to have the lowest energy consumption per 32-bit arithmetic logic unit, in comparison to other beyond-CMOS logic proposals [13].

A well-established device to study the (I)SHE is spin absorption in a lateral spin valve (LSV) where, with a non-local configuration, a pure spin current is injected from a ferromagnet (FM) electrode into a nonmagnetic transport channel and detected in a spin-orbit material (SOM) electrode [7,8,11,21,22]. Using pure spin currents is convenient for the quantification of the SHE, as it eliminates spurious signals associated with local effects. In contrast, for a potential application, such as MESO logic, LSVs present the disadvantage of a strong reduction of the spin signal caused by the exponential decay of the spin current and shunting of the generated charge current in the transport channel [23], as well as spin backflow in the FM electrode. A way to overcome these issues is by removing the transport channel and injecting and detecting the spin current directly at the FM/SOM interface. Such simpler FM/SOM T-shaped nanostructures are used to study the spin properties of HMs [10,18,24–26] and topological insulators [27] and can induce spin Hall signals 3 orders of

*f.casanova@nanogune.eu

magnitude larger in comparison with signals in LSVs. The spin Hall signals in FM/SOM T-shaped nanostructures are easily measurable at room temperature and, furthermore, this device configuration allows for independent scalable readout, in terms of voltage and current [18], which makes it ideal for magnetic state readout in the MESO logic device. However, the local electronic measurement configuration in these devices, exploiting spin-polarized currents instead of pure spin currents, might give rise to spurious transverse voltages. The Hall effects that strongly emulate the (I)SHE are the anomalous Hall effect (AHE) [28] and the planar Hall effect (PHE) [29]. An understanding of different spurious effects in the FM/HM T-shaped nanostructures, which allows for disentanglement of the proper SHE, is relevant for the reliability of magnetic state readout and the realization of the MESO logic device.

Here, we disentangle the Hall effects that could contaminate the spin Hall signal when measuring the ISHE in FM/HM nanostructures due to (1) misalignment of the magnetization and charge current in the planar direction, and (2) vertical lines in the inhomogeneous charge-current-density distribution at the FM side of the injection region. The former induces the PHE in the FM, whereas the latter can lead to the AHE in the FM. We identify that the PHE induces a shift of the baseline of the transverse resistance and distorts its shape, but does not affect the magnitude of the spin Hall signal, that is, the difference in resistance between the two magnetization directions of the FM. In contrast to the PHE case, the AHE appears with the same symmetry as the ISHE, and therefore, disentanglement from the spin Hall signal is not straightforward. However, by combining electrical measurements and a three-dimensional finite-element-method (3D FEM) simulation, the AHE contribution to the measured signal can be estimated. Further modeling shows that the AHE contribution can be minimized by tuning the thicknesses of the FM and HM electrode in the nanostructure. We find that the AHE accounts for less than 10% of the measured signal for the $\text{Co}_{50}\text{Fe}_{50}$ (15 nm)/Pt(8 nm) sample used here. Our results show that spurious Hall effects in FM/HM T-shaped nanostructures can be distinguished and minimized. Therefore, these devices can be used as a simple tool to measure the spin Hall signal to extract the spin-to-charge conversion efficiency of the system, as well as a reliable method for the readout of in-plane magnetic states [18].

II. EXPERIMENTAL DETAILS

The FM/HM nanostructures consist of a T-shaped HM nanostructure and an FM electrode, where the tip of the ferromagnetic nanowire is overlapping with the intersection of the T-shaped nanostructure, see Figs. 1(a) and 1(b) for scanning electron microscopy (SEM) images of the device. In this study, we will use Pt as the HM and $\text{Co}_{50}\text{Fe}_{50}$ (hereafter named CoFe) as the ferromagnetic material.

The devices are fabricated on SiO_2 (150 nm)/Si substrates in two steps, each step involving electron-beam lithography (EBL), metal deposition, and a lift-off process. The first step defines the T-shaped nanostructure by EBL, followed by Pt deposition via magnetron sputtering (1.3 Å/s, $p_{\text{Ar}} = 3 \times 10^{-3}$ Torr, $P = 80$ W, $p_{\text{base}} \sim 5 \times 10^{-8}$ Torr at room temperature). After lift-off, Ar-ion-beam milling is performed at grazing incidence to remove side walls on the Pt electrode. In a second EBL step, the ferromagnetic nanowire is patterned. Before CoFe deposition, Ar-ion-beam milling is performed at normal incidence to clean the Pt surface and guarantee a highly transparent interface between the Pt and CoFe electrodes. Lastly, CoFe is deposited by magnetron sputtering (0.24 Å/s, $p_{\text{Ar}} = 2 \times 10^{-3}$ Torr, $P = 30$ W, $p_{\text{base}} \sim 5 \times 10^{-8}$ Torr at room temperature) and subsequently lifted off in acetone.

The width and thickness of the Pt and CoFe electrodes for the device presented here are $w_{\text{CoFe}} = 185$ nm, $t_{\text{CoFe}} = 15$ nm, $w_{\text{Pt}} = 215$ nm, and $t_{\text{Pt}} = 8$ nm. The resistivities are measured to be $\rho_{\text{CoFe}} = 91 \mu\Omega \text{ cm}$ and $\rho_{\text{Pt}} = 154 \mu\Omega \text{ cm}$. The electrical transport measurements are performed in a physical property measurement system from Quantum Design, where we apply an in-plane magnetic field with a superconducting solenoid magnet at 300 K. The measurements are executed using the “dc reversal technique” with a Keithley 2182 nanovoltmeter and 6221 current source.

III. RESULTS AND DISCUSSION

A. Spin Hall effect and inverse spin Hall effect

Figures 1(a) and 1(b) show top-view SEM images of the device with the configurations of the ISHE and SHE measurement setups, respectively. The magnetization, \mathbf{m} , of the CoFe electrode is aligned along the easy axis of the electrode defined by shape anisotropy and can be switched with an external magnetic field, H_x . The ISHE is measured by applying a bias current, I_{bias} , from the CoFe electrode into the Pt electrode, which injects a spin current into Pt, polarized in the x direction. The strong SOC in Pt allows for the ISHE to produce a transverse charge current, which can be detected as a voltage, V_T^{ISHE} , under open-circuit conditions along the transverse Pt electrode. The reversal of \mathbf{m} induces a sign change of V_T^{ISHE} . In the SHE configuration, I_{bias} is applied through the transverse Pt electrode such that a spin-current polarized in the x direction is generated via the SHE, resulting in spin accumulation at the surfaces of the Pt. The top surface can be probed with the FM electrode, as the Fermi level of the CoFe electrode aligns with the electrochemical potential of the majority (minority) spins of spin accumulation and a positive (negative) interface voltage, V_T^{SHE} , is created when \mathbf{m} is oriented along $+x$ ($-x$) [10,18]. The spin Hall resistance is defined as $R_T^{(\text{I})\text{SHE}} = V_T^{(\text{I})\text{SHE}}/I_{\text{bias}}$. The two resistance states can be associated with the magnetic state of the ferromagnet (i.e.,

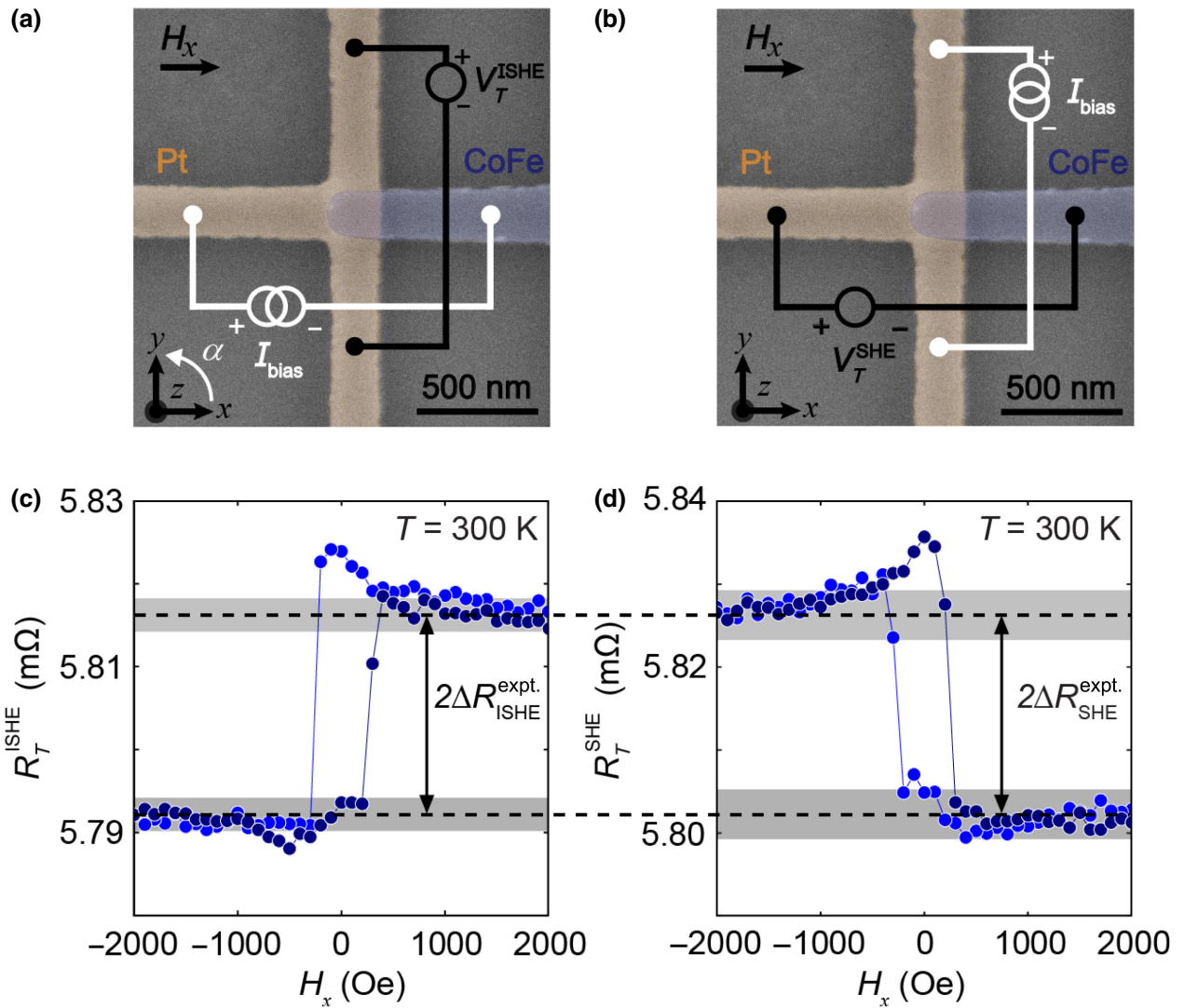


FIG. 1. (a),(b) False-colored top-view SEM images of a FM/HM nanostructure with ISHE and SHE measurement configurations, respectively, and orientation of the external magnetic field H_x . Blue indicates the CoFe electrode and yellow marks the T-shaped Pt nanostructure. (c),(d) Evolution of the transverse resistance (R_T^{ISHE} in ISHE configuration and R_T^{SHE} in SHE configuration, respectively) as a function of H_x (trace and retrace) measured at $I_{\text{bias}} = 50 \mu\text{A}$ and 300 K. Difference between low- and high-resistance states (dashed black lines; gray shaded area represents associated error) is the experimentally obtained spin Hall signal $2\Delta R_{(\text{I})\text{SHE}}^{\text{expt.}}$.

we are reading out the magnetic state) and the difference between these two resistance states is the spin Hall signal, $2\Delta R_{(\text{I})\text{SHE}}$.

Figures 1(c) and 1(d) present the transverse resistance, R_T , as a function of H_x for the ISHE and SHE measurement configurations, respectively. Figure 1(c) shows that, as long as magnetization is aligned along the $+x$ direction, the ISHE induces a constant R_T^{ISHE} , which is the high-resistance state. The reversal of magnetization to $-x$ direction by sweeping H_x switches R_T^{ISHE} to a constant low-resistance state. The same behavior is observed when sweeping H_x in the opposite direction, with a hysteresis associated with magnetization of the CoFe

electrode aligned along its easy axis. If we assume that the overall observed signal purely comes from the ISHE, we extract a spin Hall signal $2\Delta R_{\text{ISHE}}^{\text{expt.}} = (24 \pm 2) \text{ m}\Omega$. Figure 1(d) presents the transverse resistance, R_T^{SHE} , for the SHE measurement configuration, which gives $2\Delta R_{\text{SHE}}^{\text{expt.}} = (24 \pm 3) \text{ m}\Omega$. The spin Hall signals of the ISHE and the SHE are the same, as expected from the Onsager reciprocity [21]. The study in the remainder of this paper is focused on the ISHE, but the results are also valid for the SHE (see Appendix A).

The ISHE in FM/HM nanostructures can be described by the one-dimensional (1D) spin diffusion model. Notably, here, we study the CoFe/Pt system, but the

model can be extended to other FM/HM systems with transparent interfaces. If the thicknesses of the Pt and CoFe electrodes are much larger than the corresponding spin-diffusion lengths, the spin Hall signal is given by $\Delta R_{(1)SHE} = G \times \lambda_{\text{eff}}$, with a ‘‘geometrical factor’’, $G = 1/[(t_{\text{CoFe}}/\rho_{\text{CoFe}} + t_{\text{Pt}}/\rho_{\text{Pt}})w_{\text{Pt}}]$, and an ‘‘efficiency factor’’, $\lambda_{\text{eff}} = P_{\text{CoFe}}\theta_{\text{SH}}\lambda_{\text{Pt}}/(1 + \lambda_{\text{Pt}}\rho_{\text{Pt}}/\lambda_{\text{CoFe}}\rho_{\text{CoFe}}^*)$ [18]. Here, P_{CoFe} is the polarization of CoFe and $\rho_{\text{CoFe}}^* = \rho_{\text{CoFe}}(1 - P_{\text{CoFe}}^2)$. θ_{SH} is the spin Hall angle of Pt, and λ_{Pt} and λ_{CoFe} are the spin-diffusion lengths of Pt and CoFe, respectively. The efficiency of the FM/HM system, given by λ_{eff} , is independent of the geometry and resistivities of the materials. We find that, for the CoFe/Pt nanostructure under study, $G = (220 \pm 20)$ m Ω /nm. By combining G with the experimentally obtained spin Hall signal $2\Delta R_{\text{ISHE}}^{\text{expt}} = (24 \pm 2)$ m Ω , the efficiency of this CoFe/Pt nanostructure is estimated to be $\lambda_{\text{eff}} = (0.055 \pm 0.007)$ nm, in good agreement with the efficiency for this system determined by an extensive study on the scalability of the local devices, which shows that $\lambda_{\text{eff}}^{\text{CoFe/Pt}} = (0.05 \pm 0.01)$ nm. [18].

Even though the efficiency of the CoFe/Pt system in this nanostructure is the same as the expected efficiency presented in Ref. [13], it is of paramount importance to rule out possible spurious effects in the spin Hall signal. Since the spin Hall resistance is a transverse signal, showing the hysteresis of the FM element, any contamination in the measurement must arise from other Hall effects present in the FM. The Hall effects with the most significant magnitudes are the PHE and the AHE. These originate in the CoFe wire and may appear in the transverse signal due to electrical shunting through Pt. The contribution of these Hall effects will depend mainly on the resistivities and thicknesses of the Pt and CoFe electrodes and the interface resistance. Although the ordinary Hall effect (OHE) in Pt, in conjunction with out-of-plane fringe fields from the FM electrode tip, is also a potential source for a spurious signal, it is too weak to account for any measured signal (see Appendix B).

B. Planar Hall effect

It is known that ferromagnetic $3d$ metals and alloys possess a strong anisotropic magnetoresistance effect (AMR) due to s - d scattering processes from the conduction s state to the localized d states. The AMR is manifested as the difference in the longitudinal resistance as a response to a parallel or perpendicular orientation of \mathbf{m} with respect to the applied charge-current density \mathbf{j}_c , giving rise to two distinct resistivities, ρ_{\parallel} and ρ_{\perp} , respectively [30,31]. The same phenomenon induces a transverse resistance, known as the PHE. The behavior of the planar Hall resistivity as a function of the angle, φ , between an in-plane magnetization $\mathbf{m} = (m \cos(\varphi), m \sin(\varphi), 0)$ and \mathbf{j}_c is

[32,33]

$$\rho_{xy}^{\text{PHE}}(\varphi) = (\rho_{\parallel} - \rho_{\perp}) \cos(\varphi) \sin(\varphi) = \frac{(\rho_{\parallel} - \rho_{\perp})}{2} \sin(2\varphi). \quad (1)$$

This means that the PHE does not influence the spin Hall signal in our device, except in the presence of a finite in-plane angle between I_{bias} and \mathbf{m} of the CoFe electrode, as shown in Fig. 2(a). This could occur due to an angular misalignment in the experimental setup and/or in the nanofabrication.

To disentangle the PHE from the obtained spin Hall signal, the measurement configuration of the ISHE measurement setup [Fig. 1(a)] is used with an external magnetic field fixed at 5 kOe, while an in-plane rotation α of the device is performed. Since this field is large enough to overcome the shape anisotropy of the CoFe electrode, \mathbf{m} will align with the field direction. In the measurement setup, an ISHE contribution will arise from the spin current polarized along the x direction, which is proportional to $m \cos(\varphi)$. The contribution of the PHE will be proportional to $\sin(2\varphi)$ [Eq. (1)]. Hence, the dependence of the total transverse resistance on rotation angle α is described by

$$R_T^{\text{ISHE}} = R_{\text{ISHE}} + R_{\text{PHE}} + b = a_{\text{ISHE}} \cos(\alpha + \alpha_0) + a_{\text{PHE}} \sin[2(\alpha + \alpha_0)] + b, \quad (2)$$

where a_{ISHE} and a_{PHE} are the amplitudes of the ISHE and PHE, respectively; α_0 is a misalignment angle; and b is the baseline resistance of the measurement. The ISHE and the PHE can thus be identified from the difference in the angular-dependent behavior of the transverse resistances, R_{ISHE} and R_{PHE} , respectively.

Figure 2(b) shows the experimental transverse resistance as a function of α (black solid dots) together with fitting of the data to Eq. (2) (dashed red curve). The obtained fitting parameters are $a_{\text{ISHE}} = (11.8 \pm 0.7)$ m Ω , $a_{\text{PHE}} = -(99.3 \pm 0.7)$ m Ω , $\alpha_0 = -(1.0 \pm 0.2)^\circ$, and $b = (5.8001 \pm 0.0005)$ Ω . The angle α_0 has a small and realistic value for misalignment between the applied magnetic field and the CoFe nanowire that depends on the placement of the sample in the measurement setup. The contributions of the ISHE and PHE to fitting are also presented in Fig. 2(b) as the blue and cyan curves, respectively, showing that the PHE resistance has a much higher amplitude than that of the ISHE resistance. Figure 2(c) displays a magnification of the ISHE contribution from which we identify the PHE resistance, $R_{\text{PHE}}^0 = R_{\text{PHE}}^{180^\circ} = (3.5 \pm 0.7)$ m Ω , due to the presence of misalignment, whereas the ISHE resistance is $R_{\text{ISHE}}^0 = (11.8 \pm 0.7)$ m Ω and $R_{\text{ISHE}}^{180^\circ} = -(11.8 \pm 0.7)$ m Ω . The cyan dashed line represents the contribution of the PHE when α is 0° and

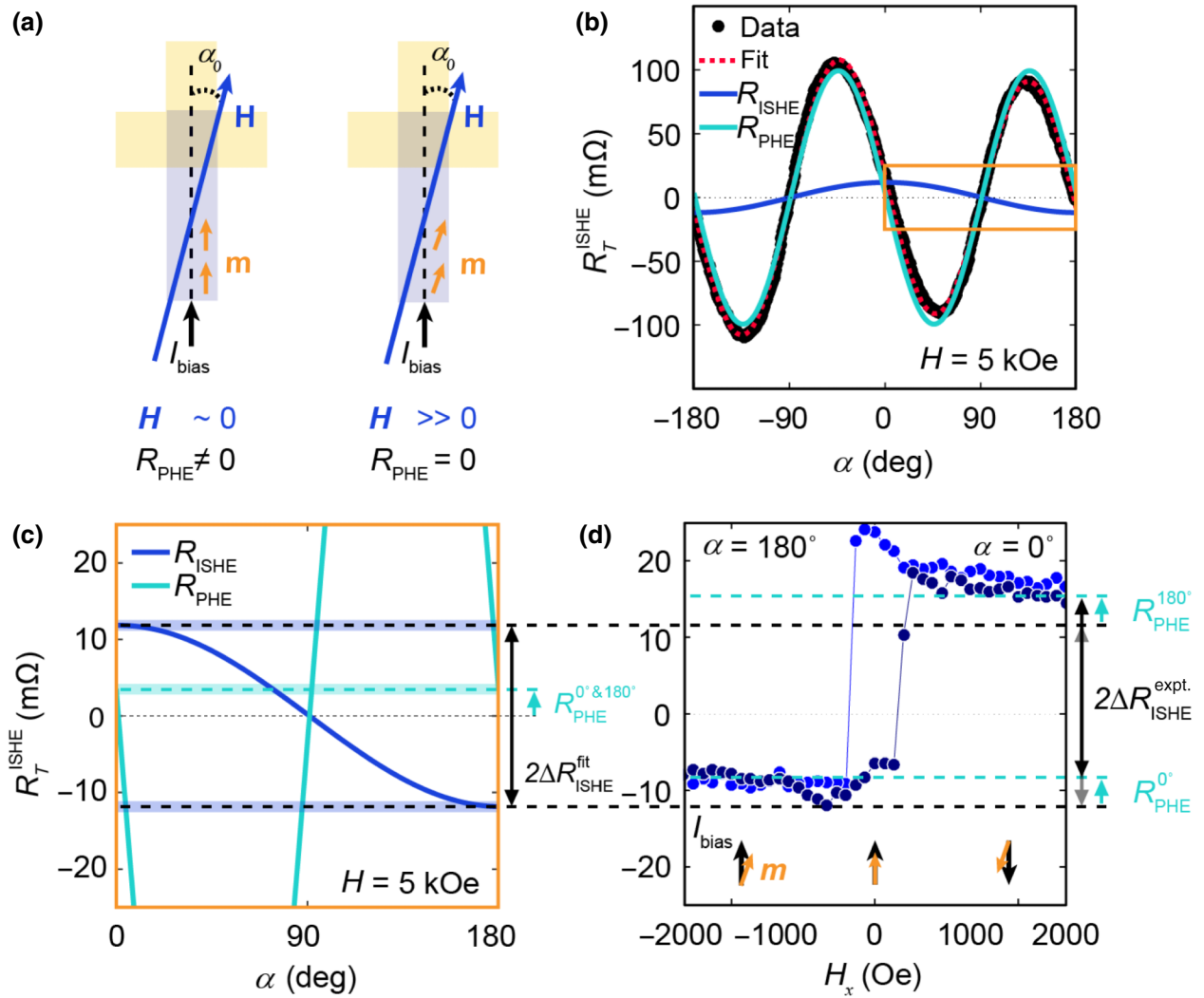


FIG. 2. (a) Representation of a FM electrode with magnetization \mathbf{m} and the effect on \mathbf{m} of misalignment angle α_0 between the applied current bias I_{bias} and an external in-plane magnetic field \mathbf{H} . Left panel: At small \mathbf{H} , \mathbf{m} aligns with the easy axis (i.e., longest dimension of the FM electrode), which is parallel to I_{bias} , such that $\varphi = 0$ and the PHE contribution is zero. Right panel: At large \mathbf{H} , \mathbf{m} aligns with \mathbf{H} , such that $\varphi = \alpha_0$ and the PHE contribution is nonzero. (b) Transverse resistance $R_T^{\text{ISHE}}(\alpha)$ as a function of the in-plane angle α [Fig. 1(a)] at $I_{\text{bias}} = 50 \mu\text{A}$ and 300 K with a fixed magnetic field of 5 kOe. Black solid dots are measured data, whereas the red dashed line indicates fitting to Eq. (2). Fit can be separated into an ISHE component and a PHE component, as shown by blue and cyan curves, respectively. (c) Magnification of the ISHE component presented in (b) indicated by the orange square. Cyan dashed line presents the magnitude of the PHE signal at $\alpha = 0^\circ$ and $\alpha = 180^\circ$ ($R_{\text{PHE}}^{0^\circ \& 180^\circ}$). (d) Transverse resistance R_T^{ISHE} versus applied magnetic field in the x direction, as given in Fig. 1(c) after subtraction of the baseline obtained from the fit ($b = 5.8001 \Omega$). High-resistance state corresponds to $\alpha = 0^\circ$, whereas low-resistance state corresponds to $\alpha = 180^\circ$. Shift of the transverse resistance by an amount of $R_{\text{PHE}}^{0^\circ \& 180^\circ}$ (cyan dashed line) is observed at large magnetic fields, where \mathbf{m} and I_{bias} are misaligned. Experimental spin Hall signal $2\Delta R_{\text{ISHE}}^{\text{expt.}}$ is the same as the spin Hall signal obtained from fitting of the angle dependence of the transverse resistance $2\Delta R_{\text{ISHE}}^{\text{fit}}$.

180° ($R_{\text{PHE}}^{0^\circ \& 180^\circ}$). The black dashed lines depict the difference between $R_{\text{ISHE}}^{0^\circ}$ and $R_{\text{ISHE}}^{180^\circ}$, i.e., the expected spin Hall signal from fitting, $2\Delta R_{\text{ISHE}}^{\text{fit}}$, which should correspond to $2\Delta R_{\text{ISHE}}^{\text{expt.}}$ measured in the magnetic field dependence. Appendix A presents an analysis of the SHE configuration, showing the same behavior for the PHE resistance.

Figure 2(d) shows the magnetic field dependence of R_T^{ISHE} , the raw data of which are plotted in Fig. 1(c), after

the baseline b , obtained from fitting, is subtracted. The positive and negative externally applied magnetic fields correspond to the angles 0° and 180° , respectively, in the angle dependence [Fig. 2(c)]. The value of $2\Delta R_{\text{ISHE}}^{\text{expt.}} = (24 \pm 2) \text{ m}\Omega$, as determined by the magnetic field dependence at high magnetic field, is observed to be the same as that obtained from the angle dependence [$2\Delta R_{\text{ISHE}}^{\text{fit}} = (24 \pm 1) \text{ m}\Omega$], but shifted because of the PHE by an

amount of $R_{\text{PHE}}^{0^\circ \& 180^\circ}$. Hence, for a negative misalignment angle, at negative and positive saturation fields, the low- and high-resistive states are given by $(-R_{\text{ISHE}} + R_{\text{PHE}})$ and $(R_{\text{ISHE}} + R_{\text{PHE}})$, respectively. In the case of positive α_0 in this configuration, the PHE resistance would be negative and would shift the transverse resistance down (for more details, see Appendix C). We note that, as the PHE has the same contribution ($+R_{\text{PHE}}$) to the negative and positive magnetic fields, $R_{\text{ISHE}}^{\text{ISHE}}$ is shifted, but the extraction of $2\Delta R_{\text{ISHE}}$ is not contaminated by the PHE.

C. Anomalous Hall effect

The AHE is the transverse deflection of charge carriers, leading to a transverse voltage observed in materials with a net magnetization when a charge current is applied [28]. This effect is generally measured in a Hall cross with an out-of-plane magnetic field (H_z). Although, in our measurement configuration, the applied magnetic field in the FM/HM nanostructures is in plane (H_x), the AHE can be present due to an inhomogeneous distribution of the charge-current density near the CoFe/Pt interface.

Unlike the case of the PHE, the symmetry of the AHE and the SHE is the same, and thus, the two contributions cannot be disentangled through an angular-dependent measurement. Therefore, 3D FEM simulations, within the framework of the two-current drift-diffusion model [34, 35], are performed to retrieve the ISHE and AHE contributions to the total transverse resistance measured in the ISHE configuration [$2\Delta R_{\text{ISHE}}^{\text{expt.}}$, see Figs. 1(a) and 1(c)]. The geometrical construction and 3D mesh [Fig. 3(a)] are elaborated using the free software GMSH [36] with the associated solver GETDP [37] for calculations, postprocessing, and data-flow control. The top CoFe/Pt interface is assumed to be transparent with no spin-memory loss and the lateral CoFe/Pt interface is considered to be insulating, as the lateral side of Pt is not etched [10,18]. Furthermore, the spin polarization of CoFe and the spin Hall angle of Pt are set to $P_{\text{CoFe}} = 0.48$ [38] and $\theta_{\text{SH}} = 0.27$ [7], respectively. We assume that $\rho_{\text{Pt}}\lambda_{\text{Pt}} = 0.77 \text{ f}\Omega \text{ m}^2$ [39] and $\rho_{\text{CoFe}}\lambda_{\text{CoFe}} = 1.29 \text{ f}\Omega \text{ m}^2$ [38], such that, considering the resistivities of our Pt and CoFe electrodes, the spin-diffusion lengths are $\lambda_{\text{Pt}} = 0.5 \text{ nm}$ and $\lambda_{\text{CoFe}} = 1.4 \text{ nm}$.

Figure 3(a) shows the electric potential in the FM/HM nanostructure when applying I_{bias} from port 1 to port 2 of the model. The inset of Fig. 3(a) shows a side view of our nanostructure with the distribution and orientation of the charge-current density in the CoFe/Pt interface region. The charge-current density possesses a component in the z direction inside the CoFe electrode, perpendicular to the in-plane magnetization (x direction). This can induce a transverse voltage in the y direction due to the AHE with the same symmetry in the magnetic hysteresis loop as that of the ISHE. The transverse signal is the difference

in electric potential between port 3 and port 4, which is normalized by the applied current.

The anomalous Hall angle $\theta_{\text{AH}} = \rho_{\text{AH}}/\rho_{\text{CoFe}}$, which quantifies the strength of the AHE in materials, serves as an input parameter for the 3D FEM and is experimentally obtained using a standard Hall cross (HC) measurement. The inset of Fig. 3(b) presents a SEM image of a CoFe Hall cross, next to our CoFe/Pt nanostructure [Figs. 1(a) and 1(b)], with the measurement configuration. A transverse voltage (V_{xy}^{HC}) appears when applying a bias current I_{bias} along the horizontal electrode and an external out-of-plane magnetic field (H_z). Figure 3(b) plots the transverse resistivity, $\rho_{xy}^{\text{HC}} = (V_{xy}^{\text{HC}}/I_{\text{bias}})t_{\text{CoFe}}$, as a function of H_z . The dashed lines are linear fits to the transverse resistivity under a large magnetic field, corresponding to the ordinary Hall contribution, and the difference between the zero-field extrapolations of the two fits is twice the anomalous Hall resistivity, $2\rho_{\text{AHE}}$. We find that the anomalous Hall resistivity of CoFe in this nanostructure is $\rho_{\text{AHE}} = (0.562 \pm 0.001) \mu\Omega \text{ cm}$, such that the anomalous Hall angle yields $(0.618 \pm 0.001)\%$.

This experimental θ_{AH} is implemented in the 3D FEM to extract the AHE contribution to the transverse signal. We define $2\Delta R_{\text{AHE}}$ as the difference between the transverse resistance induced by the AHE in the ISHE configuration at positive and negative saturated magnetization. As the magnetic hysteresis loops of the ISHE and the AHE are equal, the transverse resistance is the addition of the two contributions, i.e., $2\Delta R_{\text{ISHE}}^{\text{expt.}} = 2\Delta R_{\text{ISHE}} + 2\Delta R_{\text{AHE}}$. Finally, from the 3D FEM, we extract the spin Hall signal and the AHE contribution to be $2\Delta R_{\text{ISHE}} = (18 \pm 2) \text{ m}\Omega$ and $2\Delta R_{\text{AHE}} = 2.1 \text{ m}\Omega$, respectively. According to the 3D FEM, we should thus measure $2\Delta R_{\text{ISHE}}^{\text{expt.}} = (20 \pm 2) \text{ m}\Omega$. The FM/HM interface in our nanostructures might not be as perfectly transparent as assumed in the 3D FEM simulation; this may lead to a small increase of the experimental spin Hall signal, but, indeed, the spin Hall signal obtained from the 3D FEM is, within error, in agreement with the spin Hall signal that is experimentally measured [$2\Delta R_{\text{ISHE}}^{\text{expt.}} = (24 \pm 2) \text{ m}\Omega$].

Finally, from the simulations, we find that the AHE contribution to the total spin Hall signal is about 10% for the CoFe/Pt nanostructure under study. However, this contamination can be reduced by adjusting the thickness of the CoFe electrode. The magnitude of the z component of the charge-current density in CoFe depends on the thicknesses of the CoFe electrode and the Pt electrode. 3D FEM simulations, as discussed above, are performed for various CoFe thicknesses to extract the dependence of the AHE signal, considering the other parameters in the model system to be unchanged. Figure 3(c) shows that the AHE contribution to the measured signal can be positive or negative, depending on the thickness of the CoFe electrode. This can be understood by considering the modeled charge-current-density distribution, \mathbf{j}_c ,

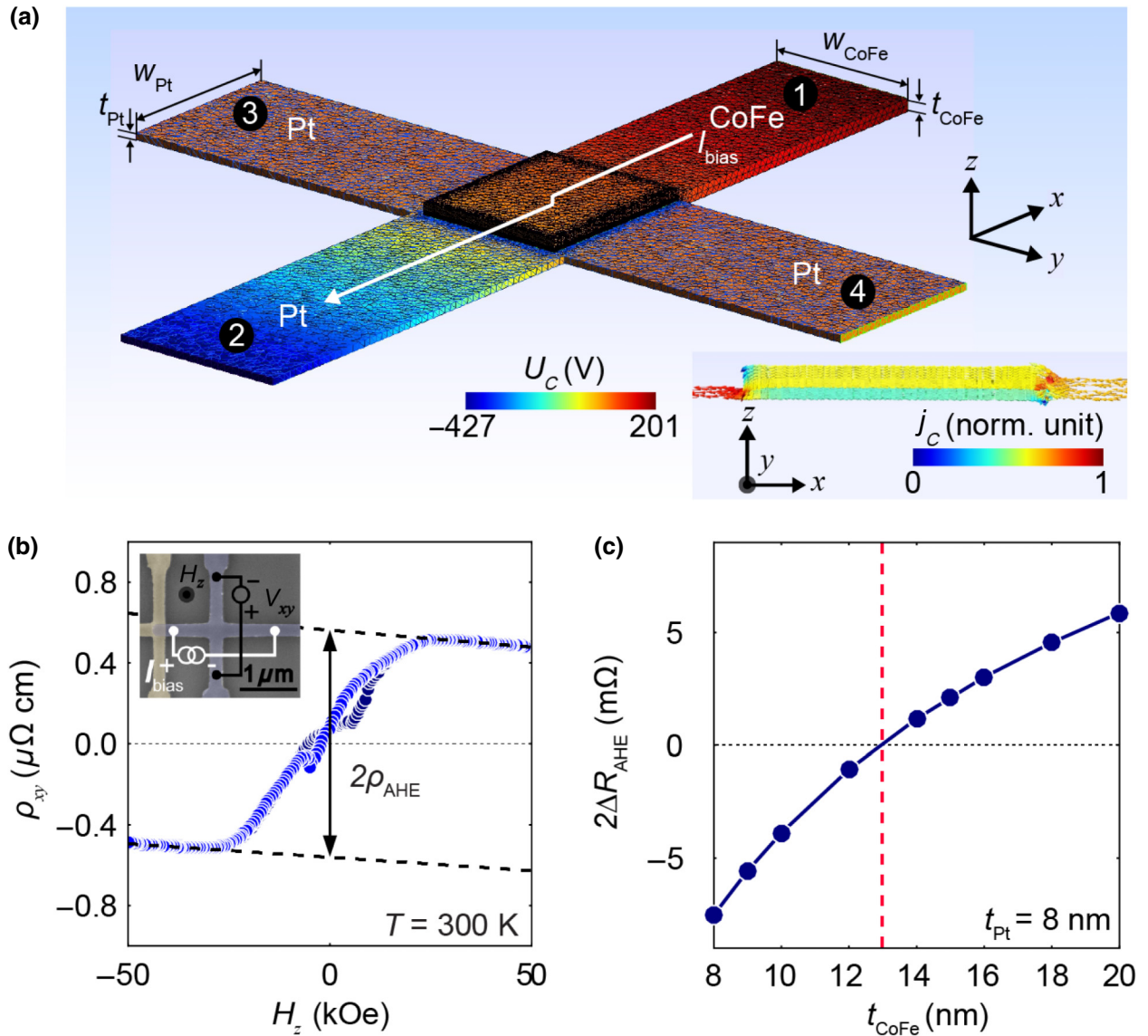


FIG. 3. (a) Geometry, mesh, and electric potential map of 3D FEM model used for the FM/HM nanostructure to estimate the AHE in the ISHE configuration. 3D color map of electrical potential induced by a bias current I_{bias} (white arrow) forced from the CoFe electrode (port 1) to the Pt electrode (port 2). As all equations used for simulations are linear, voltage values correspond to an injected current arbitrarily set at 1 A. Inset: Side view of the device (x - z plane) picturing the charge-current density lines. It shows the existence of a z component in charge-current density, which gives rise to the AHE in the CoFe electrode. (b) Out-of-plane magnetic field dependence of transverse resistivity in a CoFe cross-shaped nanostructure. Anomalous Hall resistivity ρ_{AHE} extracted from this measurement is used to determine the strength of the AHE. Inset: AHE measurement setup with the CoFe Hall cross depicted in blue. (c) CoFe electrode-thickness dependence of the AHE signal obtained using 3D FEM simulations. Line is a guide to the eye. AHE can be eliminated by optimizing the thickness of the CoFe electrode. Optimum CoFe thickness at which the AHE contribution vanishes is about 13 nm (red dashed line) in this device with a Pt electrode thickness of 8 nm and resistivities as presented in the text.

presented in the inset of Fig. 3(a). At the tip of the CoFe electrode [left side of Fig. 3(a)], \mathbf{j}_c is observed to have components oriented in the $-z$ direction, while, in the area where the CoFe electrode starts to overlap with the Pt electrode (right side), \mathbf{j}_c is oriented in the $+z$ direction. The two orientations of the charge-current density induce opposite AHE resistances that compete with one another. The

charge-current-density distribution at the interface between the Pt and CoFe electrode depends on the thicknesses of both electrodes, and thus, the two AHE contributions can be compensated for by a suitable device geometry. The contribution of the AHE, according to our simulations, is eliminated when the CoFe thickness is about 13 nm for an 8-nm-thick Pt nanowire (red dashed line). Choosing

the thickness of the FM electrode to be about 1.5 times the thickness of the HM electrode ($t_{\text{FM}} \sim 1.5 t_{\text{HM}}$) can be taken as a rule of thumb to minimize the AHE when the FM and HM resistivities are of the same order.

The different Hall effects discussed here for CoFe and Pt are present in any metallic FM (PHE and AHE) and HM (OHE); therefore, the method to disentangle these Hall effects shown in this work can be applied to any other metallic FM/HM system with a transparent interface.

IV. CONCLUSIONS

We study the appearance of spurious Hall effects in the local CoFe/Pt T-shaped nanostructures that are promising for magnetic state readout via (I)SHE measurements. The strongest Hall effects are induced in the FM electrode (PHE and AHE) and transferred into the HM electrode, whereas the OHE in the HM caused by stray fields of the FM electrode is negligible. The PHE appears with a different symmetry from that of the ISHE such that an angle misalignment between the magnetic field and the FM electrode can induce a shift in the transverse resistance. This PHE shift can be obtained and corrected for by performing a full angular-dependent measurement of the transverse resistance. The PHE contribution, however, does not affect the reading of the spin Hall signal at saturated magnetic fields. The AHE, however, appears with the same symmetry as that of the (I)SHE in the measurement. These two contributions can be disentangled by 3D FEM simulations. We observe an AHE contamination of 10% of the transverse resistance in our sample. Further investigation shows that optimizing the thickness of the CoFe electrode with respect to the Pt electrode minimizes the AHE contribution. As the one-dimensional spin-diffusion model accounts for any FM/HM system and the PHE and AHE are valid for all metallic ferromagnets, the results can be generalized to any metallic FM/HM T-shaped device. Finally, we emphasize that the FM/HM T-shaped nanostructures are an appropriate tool to measure the (I)SHE, in which the parasitic effect can be eliminated by proper alignment and optimized design of the nanostructures and are thus a viable option for future energy-efficient spin-based logic technology.

ACKNOWLEDGMENTS

This work is supported by the Intel Corporation through the Semiconductor Research Corporation under MSR-INTEL TASK No. 2017-IN-2744 and the “FEINMAN” Intel Science Technology Center, and by the Spanish MICINN under the Maria de Maeztu Units of Excellence Programme (Project No. MDM-2016-0618) and under project No. RTI2018-094861-B-100. V.T.P. acknowledges postdoctoral fellowship support from the “Juan de la Cierva—Formación”

programme by the Spanish MICINN (Grant No. FJCI-2017-34494). N.L. acknowledges funding from the European Union’s Horizon 2020 research and innovation program under the Marie Słodowska Curie Grant No. 844304 (LICONAMCO).

APPENDIX A: PHE CONTAMINATION IN THE SHE MEASUREMENT CONFIGURATION

The main text discusses how the PHE can be separated from the ISHE measurement in our CoFe/Pt nanostructures by analyzing the in-plane angle dependence of the transverse resistance. The same analysis holds true for the SHE measurement because of the Onsager reciprocity between the ISHE and the SHE [21]. Figure 4(a) presents a false-colored SEM image, showing the Pt and CoFe electrodes as the yellow and blue areas, respectively, and the SHE measurement configuration. Figure 4(b) graphs the in-plane angle dependence of the transverse resistance measured in this configuration $R_T^{\text{SHE}}(\alpha)$. The black solid dots are experimental data, and the dashed red line is the fitting to Eq. (2). The fitting parameters are $a_{\text{ISHE}} = -(10.3 \pm 0.8) \text{ m}\Omega$, $a_{\text{PHE}} = -(99.4 \pm 0.8) \text{ m}\Omega$, $\alpha_0 = -(0.9 \pm 0.2)^\circ$, and $b = -(5.8121 \pm 0.0005) \Omega$. These are comparable to the fitting parameters obtained from the ISHE measurements in the main text. The fit can be decomposed into a SHE and a PHE component due to the difference in the angle dependence, which is $\cos(\varphi)$ (blue line) and $\sin(2\varphi)$ (cyan line), respectively.

Figure 4(c) displays a magnification of the area of interest, which is the orange box in Fig. 4(b), to compare the angular dependence with the magnetic field dependence [Fig. 4(d)] of the transverse resistance. We extract the spin Hall signals as $2\Delta R_{\text{SHE}}^{\text{fit}} = (21 \pm 1) \text{ m}\Omega$ and $2\Delta R_{\text{SHE}}^{\text{expt.}} = (24 \pm 3) \text{ m}\Omega$, meaning that they are the same within the error bar. The PHE signal is $R_{\text{PHE}}^{0^\circ \& 180^\circ} = (3.1 \pm 0.8) \text{ m}\Omega$ for the SHE measurement setup. Finally, we can conclude that the fitting correctly predicts the spin Hall signal and the PHE induces a shift in the baseline, equivalent to the results shown in the main text for the ISHE.

APPENDIX B: THE ORDINARY HALL EFFECT IN THE CoFe/Pt NANOSTRUCTURE

The OHE in Pt is yet another Hall effect that could compete with the ISHE in the CoFe/Pt nanostructure. Magnetization at the tip of the CoFe electrode can induce a magnetic stray field with a z component penetrating the Pt electrode. This magnetic field, together with the current along the x axis, can yield an OHE signal along the y axis, the same one along which the ISHE is measured. The ordinary Hall resistance, which can contaminate the spin Hall signal, is $R_{xy}^{\text{OHE}} = R_H B_z / t_{\text{Pt}}$, with R_H , B_z , and t_{Pt} being the material-dependent Hall coefficient, the z component of the magnetic field in the Pt wire, and the thickness of the Pt

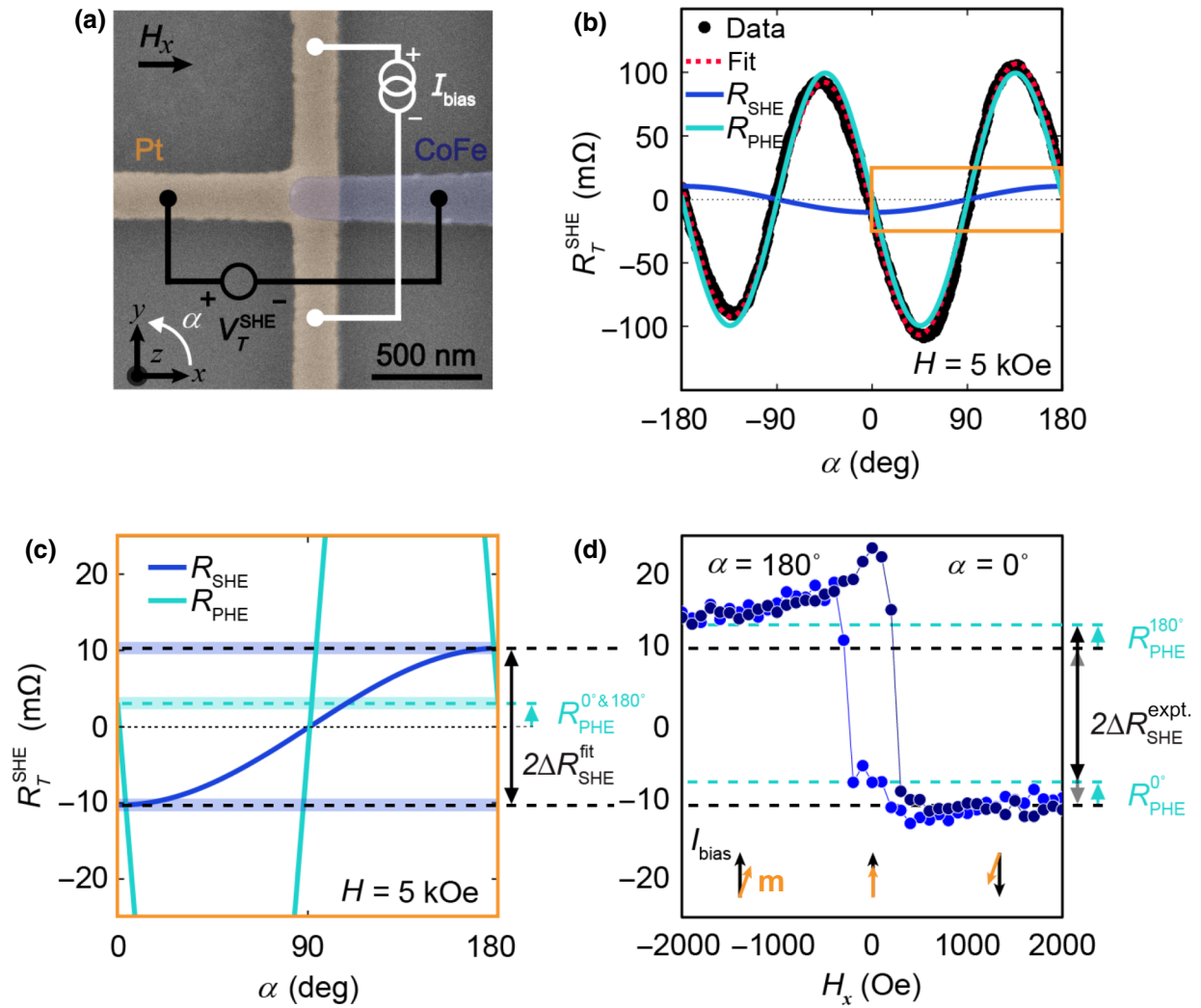


FIG. 4. (a) False-colored top-view SEM image of the FM/HM nanostructure, where the FM (CoFe) and HM (Pt) electrodes are indicated by blue and yellow, respectively. The SHE measurement configuration is displayed. The in-plane rotation of the magnetic field is described by angle α . (b) Transverse resistance R_T^{SHE} as a function of α at 300 K with a fixed magnetic field of 5 kOe. Black dots are measured data, and the red dashed line is a fit to Eq. (2). The fit is separated into an SHE component and a PHE component shown by blue and cyan curves, respectively. (c) Magnification of the ISHE component marked by the orange square in (b). The cyan dashed line presents the magnitude of the PHE signal at $\alpha = 0^\circ$ and $\alpha = 180^\circ$ ($R_{\text{PHE}}^{0^\circ \& 180^\circ}$). (d) Transverse resistance R_T^{SHE} versus applied magnetic field in the x direction, as given in Fig. 1(d) after subtraction of the baseline obtained from the fitting ($b = 5.8121 \Omega$). The low-resistance state corresponds to $\alpha = 0^\circ$, whereas the high-resistance state corresponds to $\alpha = 180^\circ$. A shift of the transverse resistance by an amount $R_{\text{PHE}}^{0^\circ \& 180^\circ}$ (cyan dashed line) is observed at large magnetic fields, where \mathbf{m} and I_{bias} are misaligned. The experimental spin Hall signal $2\Delta R_{\text{ISHE}}^{\text{expt.}}$ is the same as the spin Hall signal obtained from fitting the angle dependence to the transverse resistance $2\Delta R_{\text{ISHE}}^{\text{fit}}$.

electrode, respectively. We combine electronic Hall measurements (to obtain R_H) with micromagnetic simulation (to extract the mean stray field component $\langle B_z^{\text{stray}} \rangle$ created by the CoFe electrode) to show that the signal induced by the OHE is negligible in comparison with the ISHE.

To quantify R_H in our Pt wire, an angular-dependent Hall measurement with a fixed magnetic field (H) of 50 kOe is performed in a Hall cross of Pt that is deposited at the same time as the CoFe/Pt nanostructure,

as shown in Fig. 5(a). Figure 5(b) presents the resulting Hall resistance as a function of the out-of-plane rotation in the x - z plane (described by angle β). We assume that the OHE in our Pt is linear in the out-of-plane magnetic field, as confirmed by the excellent fit (red line) of the measurement to $R_{xy}^{\text{OHE}}(\beta) = R_{xy}^{\text{OHE}} \cos(\beta + \beta_0) + b$ with $R_{xy}^{\text{OHE}} = (15.85 \pm 0.05) \text{ m}\Omega$, $\beta_0 = -(0.5 \pm 0.2)^\circ$, and $b = -(0.43 \pm 0.03) \text{ m}\Omega$. The Hall coefficient is $R_H = R_{xy}^{\text{OHE}} t_{\text{Pt}} / B_z = (2.5 \pm 0.8) \times 10^{-11} \text{ m}^3/\text{C}$, as $t_{\text{Pt}} =$

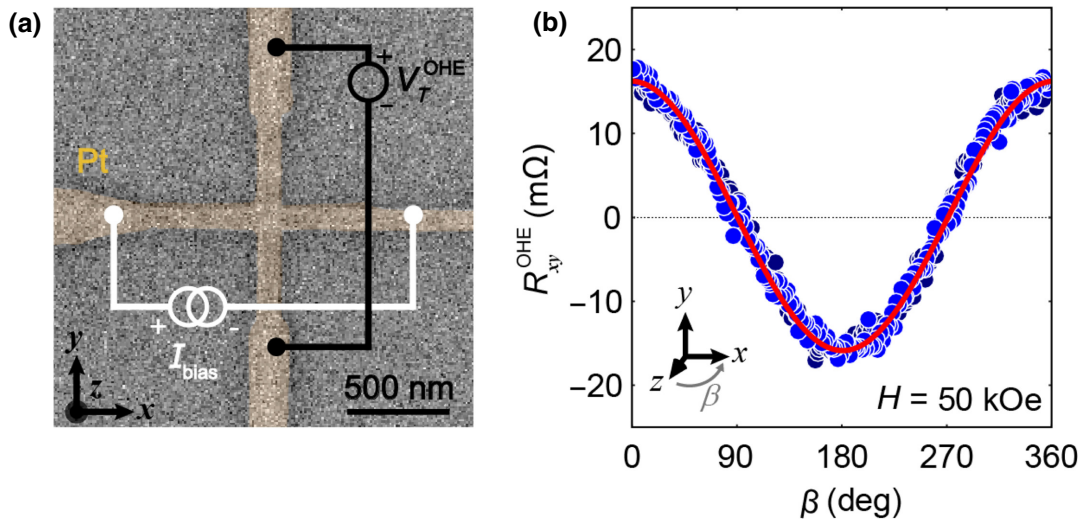


FIG. 5. (a) Ordinary Hall measurement configuration at the Pt Hall cross fabricated next to the local spin-injection device. (b) Angular dependence of the Hall resistance (R_{xy}^{OHE}) as a function of angle β with a fixed magnetic field of 50 kOe. Fitting to a $\cos(\beta)$ function is shown as a red line.

8 nm and $B_z = 5$ T is defined by a fixed value of the external magnetic field of $\mu_0 H$ (μ_0 is the vacuum permeability).

The magnitude of the stray fields originating from the CoFe electrode into the Pt electrode are determined using MUMAX³, which is an open-source software for micromagnetic simulations on graphics processing units (GPU) [40]. Figure 6(b) shows the CoFe/Pt structure used for these simulations, considering $t_{\text{Pt}} = 9$ nm, $t_{\text{CoFe}} = 15$ nm, $w_{\text{Pt}} = 215$ nm, and $w_{\text{CoFe}} = 185$ nm, which are comparable to the dimensions in the CoFe/Pt nanostructure studied in the main text. The wires are divided into a regular mesh of cuboid cells with dimensions of $3.125 \times 3.125 \times 3$ nm³. For this reason, the thickness of the Pt electrode in the simulation is chosen to be 1 nm thicker than the real electrode thickness. This, however, will not influence the result significantly, since the strongest stray field will be induced in the area closest to the FM electrode. A saturation magnetization of $M_{\text{sat}} = 1$ MA/m (the value for nonannealed CoFe) [41] and an exchange constant of $A_{\text{ex}} = 18$ pJ/m (the value for very thin Co) [42] are used for the simulations. We consider that there is no anisotropy, since our CoFe is polycrystalline.

First, we simulate the three components (x , y , and z) of magnetization in the CoFe electrode and its response to an external magnetic field sweep along the x axis to imitate the ISHE measurement. Figure 6(a) shows the average magnetization in the area where the CoFe wire overlaps with the Pt electrode versus the magnitude of the external magnetic field, showing a coercive field of $H_c \sim 950$ Oe. The average magnetization in the x direction is strongest, as expected. However, around H_c , a component in the z direction appears, while the y component stays rather

constant over the full range of external magnetic fields. Figure 6(b) presents a top view of the simulated structure, including snapshots of magnetization at two different magnetic fields around H_c , which are displayed as blue dots in Fig. 6(a).

Next, we simulate the stray field in the Pt electrode induced as a consequence of magnetization in the CoFe wire. Figure 6(c) shows that the CoFe magnetization induces an average stray field in the Pt electrode with strong components in the x direction and z direction. The z component is the one we are interested in, as it will induce a transverse resistance due to the OHE in Pt, which adds to the spin Hall signal. We find that the average stray field in the z direction reaches a maximum of $\langle B_{\text{stray},z} \rangle \sim 70$ mT close to the coercive field $H_c \sim 950$ Oe. For higher applied fields, $\langle B_{\text{stray},z} \rangle$ saturates to a value of about 25 mT. Figure 6(d) presents a top view of the CoFe/Pt nanostructure with the z component of the stray field at the intersection area of both wires.

The Hall resistance, which will appear in the ISHE measurement, i.e., that will contaminate the spin Hall signal, can be estimated by combining the Hall coefficient ($R_H = 2.5 \times 10^{-11}$ m³/C), the Pt wire thickness of t_{Pt} , and the z component of the magnetic stray field within the Pt wire. The maximum contribution of the OHE will be around the switching field, where $\langle B_{\text{stray},z} \rangle \sim 70$ mT results in an OHE resistance of 0.2 mΩ, which is insignificant. Contamination of the transverse resistance should be considered at the field of saturation, where the stray field is $\langle B_{\text{stray},z} \rangle \sim 25$ mT, which yields an OHE resistance of 0.08 mΩ. This is about 0.3% of the total transverse resistance [24 ± 2 mΩ], meaning that contamination of the ISHE with the OHE is negligible.

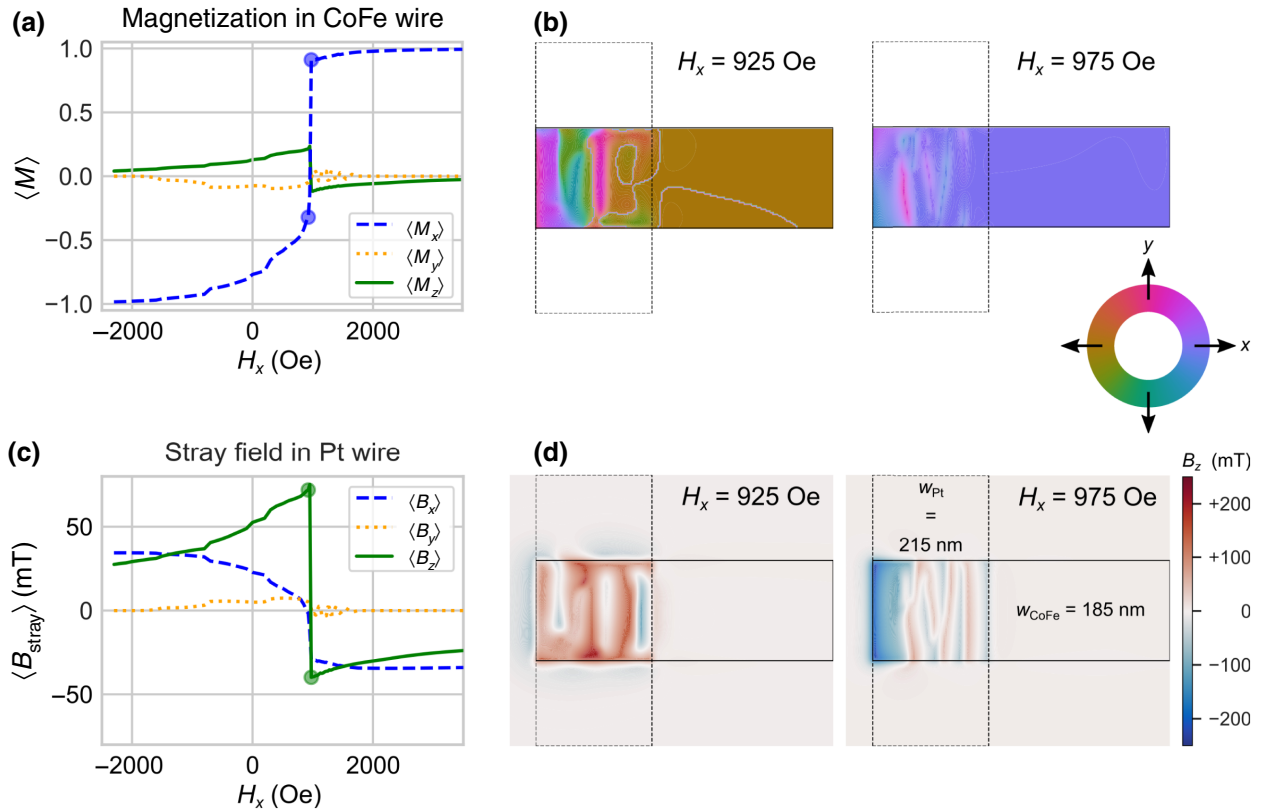


FIG. 6. (a) Simulated mean magnetization components of CoFe in the area where the CoFe wire overlaps with the Pt wire as a function of a field, H_x , applied along the CoFe wire's long axis. (b) Snapshots of the in-plane magnetization (see color wheel) at a height of $z = 9$ nm, which corresponds to the vertical middle of the CoFe electrode ($t_{\text{CoFe}} = 15$ nm, with 3 nm cell height), at specific fields during the switching of magnetization. Location of the snapshots in magnetic field are indicated by blue dots in panel (a). (c) Mean stray-field components generated in the Pt wire overlapping with the CoFe wire as a function of field H_x . The maximum value of $\langle B_{\text{stray},z} \rangle$ reaches about 70 mT and saturates to about 25 mT at high saturation fields. (d) Snapshots of the z component of the stray field in the Pt wire at $z = 21$ nm (i.e., 6 nm above the CoFe wire) evaluated at the same fields as CoFe magnetization in panel (b). Green dots in panel (c) indicate the magnetic field position of the snapshot.

APPENDIX C: EXPECTED SHAPE OF THE TRANSVERSE-RESISTANCE LOOP IN THE PRESENCE OF THE PHE

The PHE appears in the transverse resistance only if there is misalignment between the applied current I_{bias} and magnetization \mathbf{m} . In the ISHE measurement setup, \mathbf{m} is aligned along the easy axis of the FM electrode at low magnetic fields, and along the external magnetic field \mathbf{H} at high fields. Therefore, at low fields, \mathbf{m} will be parallel to I_{bias} , whereas, at high fields, a misalignment between \mathbf{m} and I_{bias} can be introduced due to positioning of the device on the sample during fabrication and/or the placement of the sample inside the measurement station. Figure 7 shows a sketch of I_{bias} , \mathbf{m} , and \mathbf{H} for negative and positive misalignment angles (α_0) in our ISHE measurement configuration.

The angle between I_{bias} and \mathbf{m} is given by $\varphi = \alpha + \alpha_0$, where α is the angle between the sample holder and \mathbf{H} defined by the equipment. For R_T^{ISHE} versus \mathbf{H}

measurements, α is set to 180° . As shown in Eq. (2), the ISHE resistance and the PHE resistance are given by $R_{\text{ISHE}} = a_{\text{ISHE}} \cos(\varphi)$ and $R_{\text{PHE}} = a_{\text{PHE}} \sin(2\varphi)$, respectively. At low magnetic field (yellow area), I_{bias} and \mathbf{m} are aligned because \mathbf{H} is not strong enough to overcome the shape anisotropy, which aligns \mathbf{m} along the easy axis of the FM electrode. In this situation, $\varphi = 0$, i.e., R_{PHE} is zero and, therefore, we have only a contribution of the ISHE resistance. However, when we increase \mathbf{H} , such that \mathbf{m} aligns with \mathbf{H} (green area), the misalignment angle is also induced between I_{bias} and \mathbf{m} ($\varphi = \alpha_0$) and R_{PHE} becomes nonzero. The PHE resistance is negative or positive, depending on whether α_0 is negative [Fig. 7(a)] or positive [Fig. 7(b)], respectively.

Figures 7(c) and 7(d) display a sketch of the transverse resistance, $R_T^{\text{ISHE}}(H)$, as a function of the magnetic field. In the ideal case, without misalignment and a vanishing PHE contribution, switching of the resistance states would be sharp and flat (square loop). However, in the presence of a misalignment angle, the shape of the R_T^{ISHE} loop is

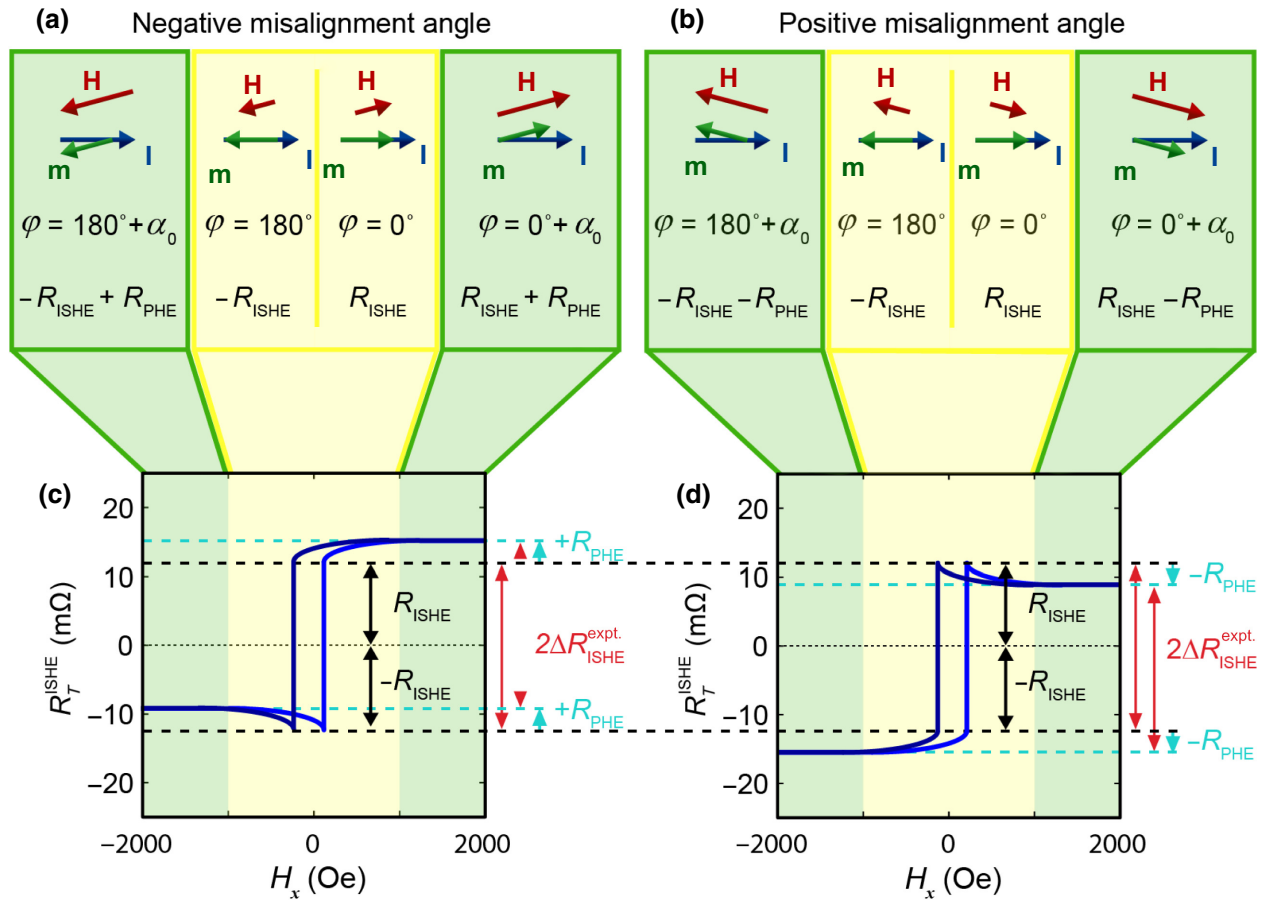


FIG. 7. Expected shape of transverse resistance $R_T^{\text{ISHE}}(H)$ loop induced by the PHE contribution. (a),(b) Sketch of alignment of current I_{bias} , magnetization \mathbf{m} , and external magnetic field \mathbf{H} at high (green areas) and low magnetic fields (yellow areas) for negative and positive misalignment angles, α_0 , between I_{bias} and \mathbf{m} . When I_{bias} and \mathbf{m} are parallel, the transverse resistance is equal to the ISHE resistance, i.e., R_{ISHE} , if no other Hall effects are involved. If there is misalignment between I_{bias} and \mathbf{H} , misalignment is transferred to \mathbf{m} above a certain threshold value of \mathbf{H} ; therefore, the PHE contribution R_{PHE} appears only at magnetic fields above this threshold value. (c),(d) $R_T^{\text{ISHE}}(H)$ loop as a function of applied magnetic field in the ISHE configuration, for negative and positive misalignment angles, respectively. Effect of the PHE on R_T^{ISHE} is twofold. First, PHE shifts the baseline signal down (negative misalignment angle) or up (positive misalignment angle). Second, PHE induces specific shapes (dips and upturns) close to the switching field of magnetization in the magnetic field dependence.

altered because of the dependence on the strength of \mathbf{H} , as discussed previously. Ideally, when sweeping \mathbf{H} from negative to positive and considering a negative misalignment angle [see Fig. 7(c)], the transverse resistance starts at a value equal to $-R_{\text{ISHE}} + R_{\text{PHE}}$, which slowly decreases to $-R_{\text{ISHE}}$ because \mathbf{m} rotates towards the easy axis of the FM electrode, that is, parallel to I_{bias} , as \mathbf{H} moves to positive values. This creates the sharp dip in the R_T^{ISHE} loop. By further increasing \mathbf{H} , \mathbf{m} switches 180° , but will be still parallel to I_{bias} , resulting in a transverse resistance of R_{ISHE} . Finally, at high magnetic field values, \mathbf{m} aligns again along \mathbf{H} and the transverse resistance obtains an additional contribution, $+R_{\text{PHE}}$. When sweeping from positive to negative magnetic field values, the $R_T^{\text{ISHE}}(H)$ curve has same shape, but is shifted by the magnetic hysteresis. Figure 7(d) shows similar behavior, although inverted because the positive

misalignment angle induces a negative PHE resistance ($-R_{\text{PHE}}$). This specific shape is not precisely observed in our experimental measurement, which is most probably related to the fact that magnetization in the tip of the FM is not perfectly aligned along the easy axis of the FM at low magnetic field, as also observed in the micromagnetic simulations in Figs. 6(a) and 6(b). Nevertheless, for both negative and positive misalignment angles, the PHE resistance has the same magnitude and sign at high positive and negative magnetic fields. Correspondingly, the spin Hall signal ($\Delta R_{\text{ISHE}}^{\text{expt.}}$) can be accurately extracted from the difference between the transverse resistance at field values above saturation of the PHE.

Notably, the sketch in Fig. 7 is made considering a material with a positive spin Hall angle, such as Pt used here. Materials with a negative spin Hall angle, such as Ta and

W, will have positive and negative R_T^{ISHE} values at negative and positive magnetic field values, respectively, opposite to Pt. However, in the presence of a misalignment angle, the PHE characteristics in the R_T^{ISHE} loop (the dips and upturns around the switching fields, as presented here for Pt) will be equally valid in negative spin Hall materials.

-
- [1] T. Kuschel and G. Reiss, Charges ride the spin wave, *Nat. Nanotechnol.* **10**, 22 (2014).
- [2] F. Hellman, A. Hoffmann, Y. Tserkovnyak, G. S. D. Beach, E. E. Fullerton, C. Leighton, A. H. Macdonald, D. C. Ralph, D. A. Arena, H. A. Durr, et al., Interface-induced phenomena in magnetism, *Rev. Mod. Phys.* **89**, 025006 (2017).
- [3] A. Manchon, H. C. Koo, J. Nitta, S. M. Frolov, and R. A. Duine, New perspectives for Rashba spin-orbit coupling, *Nat. Mater.* **14**, 871 (2015).
- [4] A. Soumyanarayanan, N. Reyren, A. Fert, and C. Panagopoulos, Emergent phenomena induced by spin-orbit coupling at surfaces and interfaces, *Nature (London)* **539**, 509 (2016).
- [5] A. Manchon, J. Železný, I. M. Miron, T. Jungwirth, J. Sinova, A. Thiaville, K. Garello, and P. Gambardella, Current-induced spin-orbit torques in ferromagnetic and antiferromagnetic systems, *Rev. Mod. Phys.* **91**, 035004 (2019).
- [6] J. Sinova, S. O. Valenzuela, J. Wunderlich, C. H. Back, and T. Jungwirth, Spin Hall effects spin Hall effects, *Rev. Mod. Phys.* **87**, 1213 (2015).
- [7] E. Sagasta, Y. Omori, M. Isasa, M. Gradhand, L. E. Hueso, Y. Niimi, Y. Otani, and F. Casanova, Tuning the spin Hall effect of Pt from the moderately dirty to the superclean regime, *Phys. Rev. B* **94**, 060412(R) (2016).
- [8] E. Sagasta, Y. Omori, S. Vélez, R. Llopis, C. Tollan, A. Chuvilin, L. E. Hueso, M. Gradhand, Y. Otani, and F. Casanova, Unveiling the mechanisms of the spin Hall effect in Ta, *Phys. Rev. B* **98**, 060410 (2018).
- [9] C.-F. Pai, L. Liu, Y. Li, H. W. Tseng, D. C. Ralph, and R. A. Buhrman, Spin transfer torque devices utilizing the giant spin Hall effect of tungsten, *Appl. Phys. Lett.* **101**, 122404 (2012).
- [10] V. T. Pham, L. Vila, G. Zahnd, A. Marty, W. Saverio-Torres, M. Jamet, and J.-P. Attané, Ferromagnetic/nonmagnetic nanostructures for the electrical measurement of the spin Hall effect, *Nano Lett.* **16**, 6755 (2016).
- [11] M. Morota, Y. Niimi, K. Ohnishi, D. H. Wei, T. Tanaka, H. Kontani, T. Kimura, and Y. Otani, Indication of intrinsic spin Hall effect in 4d and 5d transition metals, *Phys. Rev. B* **83**, 174405 (2011).
- [12] S. Manipatruni, D. E. Nikonov, and I. A. Young, Beyond CMOS computing with spin and polarization, *Nat. Phys.* **14**, 338 (2018).
- [13] S. Manipatruni, D. E. Nikonov, C.-C. Lin, T. A. Gosavi, H. Liu, B. Prasad, Y.-L. Huang, E. Bonturim, R. Ramesh, and I. A. Young, Scalable energy-efficient magnetoelectric spin-orbit logic, *Nature (London)* **565**, 35 (2019).
- [14] S.-H. C. Baek, K.-W. Park, D.-S. Kil, Y. Jang, J. Park, K.-J. Lee, and B.-G. Park, Complementary logic operation based on electric-field controlled spin-orbit torques, *Nat. Electron.* **1**, 398 (2018).
- [15] P. A. Dowben, D. E. Nikonov, A. Marshall, and Ch. Binek, Magneto-electric antiferromagnetic spin-orbit logic devices, *Appl. Phys. Lett.* **116**, 080502 (2020).
- [16] L. Liu, C.-F. Pai, Y. Li, H. W. Tseng, D. C. Ralph, and R. A. Buhrman, Spin-torque switching with the giant spin Hall effect of tantalum, *Science* **336**, 555 (2012).
- [17] I. M. Miron, K. Garello, G. Gaudin, P.-J. Zermatten, M. V. Costache, S. Auffret, S. Bandiera, B. Rodmacq, A. Schuhl, and P. Gambardella, Perpendicular switching of a single ferromagnetic layer induced by in-plane current injection, *Nature (London)* **476**, 189 (2011).
- [18] V. T. Pham, I. Groen, S. Manipatruni, W. Y. Choi, D. E. Nikonov, E. Sagasta, C.-C. Lin, T. A. Gosavi, A. Marty, L. E. Hueso, I. A. Young, and F. Casanova, Spin-orbit magnetic state readout in scaled ferromagnetic/heavy metal nanostructures, *Nat. Electron.* **3**, 309 (2020).
- [19] S. Maat and A. C. Marley, in *Handbook of Spintronics*, edited by Y. Xu, D. D. Awschalom, J. Nitta (Springer, Dordrecht, 2016), pp. 977–1028.
- [20] A. D. Kent and D. C. Worledge, A new spin on magnetic memories, *Nat. Nanotechnol.* **10**, 187 (2015).
- [21] T. Kimura, Y. Otani, T. Sato, S. Takahashi, and S. Maekawa, Room-Temperature Reversible Spin Hall Effect, *Phys. Rev. Lett.* **98**, 156601 (2007).
- [22] P. Laczkowski, Y. Fu, H. Yang, J.-C. Rojas-Sánchez, P. Noel, V. T. Pham, G. Zahnd, C. Deranlot, S. Collin, C. Bouard, P. Warin, V. Maurel, M. Chshiev, A. Marty, J.-P. Attané, A. Fert, H. Jaffrès, L. Vila, and J.-M. George, Large enhancement of the spin Hall effect in Au by side-jump scattering on Ta impurities, *Phys. Rev. B* **96**, 140405(R) (2017).
- [23] W. Yan, E. Sagasta, M. Ribeiro, Y. Niimi, L. E. Hueso, and F. Casanova, Large room temperature spin-to-charge conversion signals in a few-layer graphene/Pt lateral heterostructure, *Nat. Commun.* **8**, 661 (2017).
- [24] C. Fang, C. H. Wan, B. S. Yang, J. Y. Qin, B. S. Tao, H. Wu, X. Zhang, X. F. Han, A. Hoffmann, X. M. Liu, and Z. M. Jin, Determination of spin relaxation times in heavy metals via second-harmonic spin injection magnetoresistance, *Phys. Rev. B* **96**, 134421 (2017).
- [25] L. Liu, C. T. Chen, and J. Z. Sun, Spin Hall effect tunnelling spectroscopy, *Nat. Phys.* **10**, 561 (2014).
- [26] V. T. Pham, L. Vila, G. Zahnd, P. Noël, A. Marty, and J.-P. Attané, Cross-shaped nanostructures for the study of spin to charge inter-conversion using spin-orbit coupling in non-magnetic materials, *Appl. Phys. Lett.* **114**, 222401 (2019).
- [27] L. Liu, A. Richardella, I. Garate, Y. Zhu, N. Samarth, and C. T. Chen, Spin-polarized tunneling study of spin-momentum locking in topological insulators, *Phys. Rev. B* **91**, 235437 (2015).
- [28] N. Nagaosa, J. Sinova, S. Onoda, A. H. MacDonald, and N. P. Ong, Anomalous Hall effect, *Rev. Mod. Phys.* **82**, 1539 (2010).
- [29] J.-P. Jan, in *Solid State Physics*, edited by F. Seitz, D. Turnbull (Academic Press, New York, 1957), Vol. 5, pp.1–96.

- [30] T. R. McGuire and R. I. Potter, Anisotropic magnetoresistance in ferromagnetic 3d alloys, *IEEE Trans. Magn. MAG-11*, 1018 (1975).
- [31] S. Kokado, M. Tsunoda, K. Harigaya, and A. Sakuma, Anisotropic magnetoresistance effects in Fe, Co, Ni, Fe₄N, and half-metallic ferromagnet: A systematic analysis, *J. Phys. Soc. Japan* **81**, 024705 (2012).
- [32] A. B. Pippard, *Magnetoresistance in Metals* (Cambridge University Press, Cambridge, 1989).
- [33] Z. Li, T. Xiao, R. Zou, J. Li, Y. Zhang, Y. Zeng, M. Zhou, J. Zhang, and W. Wu, Planar Hall effect in PtSe₂, *J. Appl. Phys.* **127**, 054306 (2020).
- [34] A. Fert and I. A. Campbell, Two-Current Conduction in Nickel, *Phys. Rev. Lett.* **21**, 1190 (1968).
- [35] I. A. Campbell, A. Fert, and R. Pomeroy, Evidence for two current conduction iron, *Philos. Mag.* **15**, 977 (1967).
- [36] C. Geuzaine and J.-F. Remacle, Gmsh: A 3-D finite element mesh generator with built-in pre- and post-processing facilities, *Int. J. Numer. Methods Eng.* **79**, 1309 (2009).
- [37] C. Geuzaine, GetDP: A general finite-element solver for the de Rham complex, *Proc. Appl. Math. Mech.* **7**, 101603 (2007).
- [38] G. Zahnd, L. Vila, V. T. Pham, W. Lim, A. Brenac, P. Laczkowski, A. Marty, and J.-P. Attané, Spin diffusion length and polarization of ferromagnetic metals measured by the spin-absorption technique in lateral spin valves, *Phys. Rev. B* **98**, 174414 (2018).
- [39] M. Nguyen, D. C. Ralph, and R. A. Buhrman, Spin Torque Study of the Spin Hall Conductivity and Spin Diffusion Length in Platinum Thin Films with Varying Resistivity, *Phys. Rev. Lett.* **116**, 126601 (2016).
- [40] A. Vansteenkiste, J. Leliaert, M. Dvornik, M. Helsen, F. Garcia-Sanchez, and B. Van Waeyenberge, The design and verification of MuMax³, *AIP Adv.* **4**, 107133 (2014).
- [41] S. P. Vernon, S. M. Lindsay, and M. B. Stearns, Brillouin scattering from thermal magnons in a thin Co film, *Phys. Rev. B* **29**, 4439 (1984).
- [42] G. Shirane, V. J. Minkiewicz, and R. Nathans, Spin waves in 3d metals, *J. Appl. Phys.* **39**, 383 (1968).